Chapter 3

Electronic Theory

In the previous chapter, we described the important results brought by symmetry analysis. We have also stated its deficiences, namely the lack of quantitative conclusions. These deficiencies can be overcome by performing an electronic calculation *based upon the results of our symmetry analysis*. This electronic calculation, described in the current chapter of this work, is the next step of developing our theory of SHG from antiferromagnetic surfaces.

We set up the theory and perform our calculation having a particular material, NiO, in mind. However, taking into account the electronic configurations $3d^8$, $3d^7$, and $3d^6$ opens the way to describe properly not only the highly excited states of NiO, but also other materials. With only slight modification of this work, nearly all elements[23] of the periodic table can be addressed, which overcomes earlier limitations of that theory. Especially, the extension to other cubic metal oxides is straightforward.

Our ligand-field-theory approach allows us to fully consider the *surface* of the material. We are not restricted to a monolayer of NiO.

The results of our calculations concern the SHG response of the sample in the equilibrium state. We present the spectra of the nonlinear magneto-optical susceptibility tensor which governs this response. Furthermore, we develop a theory and perform a simulation of a pump-and-probe experiment. During such an experiment, the dynamical behavior of electrical charges and magnetic moments of antiferromagnetic NiO can be investigated on the time scale of femtoseconds.

3.1 Interplay of Symmetry and Electronic Theory

One of the important results of our symmetry analysis (Chapter 2) is the determination of the nonvanishing elements of the nonlinear optical susceptibility tensor for a given surface spin configuration. The existence or vanishing of certain tensor elements has, besides the classical covering symmetry, also microscopical reasons. Here, will discuss the interplay between these symmetry-related and microscopic origins of the nonlinear magneto-optical

[23] Systems which escape the analysis within this framework are atoms with the electronic configuration d^5 (Cr, Mn, Mo, Re), and those where valence band includes f electrons (actinides).

susceptibility tensor. The argumentation presented here applies to the (001) surface, but the extensions to other low-index surfaces can be performed without difficulties.

In general, the tensor element $\chi^{(2)}_{ijk}(2\mathbf{q}, 2\omega)$ can be expressed as follows [13, 70]:

$$\chi^{(2)}_{ijk}(2\mathbf{q},2\omega) = \frac{e^3}{2q^3V}\sum_{\mathbf{k},l,l',l''}\Bigg[\langle\mathbf{k}+2\mathbf{q},l''|i|\mathbf{k}l\rangle\langle\mathbf{k}l|j|\mathbf{k}+\mathbf{q},l'\rangle\langle\mathbf{k}+\mathbf{q},l'|k|\mathbf{k}+2\mathbf{q},l''\rangle \times \\ \times \frac{\frac{f(E_{\mathbf{k}+2\mathbf{q},l''})-f(E_{\mathbf{k}+\mathbf{q},l'})}{E_{\mathbf{k}+2\mathbf{q},l''}-E_{\mathbf{k}+\mathbf{q},l'}-\hbar\omega+i\hbar\alpha} - \frac{f(E_{\mathbf{k}+\mathbf{q},l'})-f(E_{\mathbf{k}l})}{E_{\mathbf{k}+\mathbf{q},l'}-E_{\mathbf{k}l}-\hbar\omega+i\hbar\alpha}}{E_{\mathbf{k}+2\mathbf{q},l''}-E_{\mathbf{k}l}-2\hbar\omega+2i\hbar\alpha}\Bigg], \quad (3.1)$$

where V is the volume of the unit cell (because we treat the surface, we integrate over one half of the unit cell) and f is the Fermi distribution. The screening factor has been neglected. The summation is executed over wavevectors $\mathbf{k}$ corresponding to the states l, and also over two lattice sites, with the atomic magnetic moment set antiparallely in the AF phase (staggered summation). This allows us to account for the antiferromagnetism. The damping factor α gives us the causal part of the Green's function and corresponds to the breaking of time-reversibility of the Hamiltonian. Matrix elements $\langle\mathbf{k},l|i,j,\text{or } k|\mathbf{k},l\rangle$ describe transitions between the electronic d and s states of nickel, consequently they are forbidden in the spherically symmetric environment. Breakdown of the inversion symmetry at the surface changes the selection rules, so that transitions with $\Delta l = \pm 2, \pm 1$ and 0 are allowed. We restrict ourselves to intra-atomic transitions, since they suffice to explain the spectral structures within the gap of NiO [71, 72].

Spin-orbit coupling, being mainly effective in the magnetically-ordered phases, slightly lifts the orthogonality of the wavefunctions (in addition to a similar effect produced by the surface symmetry breaking). As the result, the dipoles x, y, and z are no longer orthogonal. This allows for the non-vanishing triple product of these dipoles in eq. (3.1).

The transition matrix elements are quite cumbersome to calculate, thus in our calculations we will only use some estimates of their value according to [73]. Additionally, some of the products of the transition matrix elements can cancel depending on the symmetry of the investigated surface. In the following subsections, we will qualitatively discuss the nonvanishing tensor elements as resulting from these products for each of the magnetic phases of the surface.

3.1.1 The Paramagnetic Phase

In this magnetic phase, mainly the surface symmetry breaking plays a role in determining the transition matrix elements. The directions x and y (in-plane) are equivalent, so we do not expect any tensor elements which result from a combination of dipoles x and y. From this and because the z direction is distinguished (surface normal),

- tensor elements χ_{zxx} and χ_{zyy} should be equal, but different from χ_{zzz}, and
- in order to suppress any information about magnetization, indices x and y should be present an even number of times each.

These conditions allow for the following tensor elements: $\chi_{zxx} = \chi_{zyy}$, χ_{zzz}, and $\chi_{yyz} = \chi_{xxz}$. This is in agreement with the results of our symmetry analysis.

In the paramagnetic phase, the magnetic moments localized on nickel atoms are disordered and thus do not influence the result. Therefore, for the tensor elements which do not vanish in the paramagnetic phase, their value calculated according to eq. (3.1) is equal to a value resulting from only one nickel atom multiplied by two.

As it can be seen from the above argumentation, the paramagnetic tensor elements do not exhibit any dependence on spin-orbit coupling (to first order).

3.1.2 The Ferromagnetic Phase

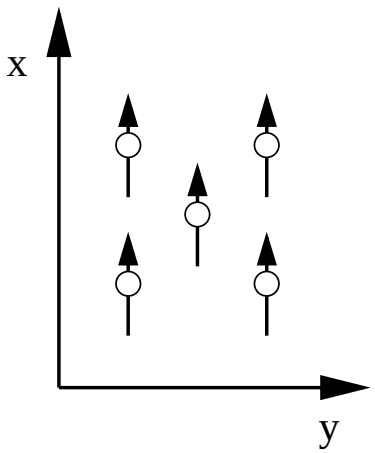

Figure 23: The ferromagnetic surface spin configuration used to perform the analysis in the current subsection.

The specific spin configuration we have in mind performing the analysis described here is shown in Fig. 23. Because the magnetic moments are parallel to the x axis, we do not expect any tensor elements containing x an odd number of times. This leaves us with the set of tensor elements described previously as paramagnetic, additionally some other tensor elements are present, we will refer to them as ferromagnetic. These ferromagnetic tensor elements contain y an odd number of times, from which we can deduce their *linear* dependence on spin-orbit coupling. Pairs of tensor elements which were equal in the paramagnetic phase, like $\chi_{zxx} = \chi_{zyy}$, are not equal now because of the ferromagnetic contribution to them. The preferential axis is namely parallel to x, which is thus inequivalent to y. Our numerical calculation is unable to determine this contribution, since it is of higher than first order in spin-orbit coupling.

The set of tensor elements deduced from the above considerations is the same as the set obtained by our symmetry analysis in the Chapter 2, for the configuration "ferro1" of the (001) surface.

3.1.3 The Antiferromagnetic Phase

Unlike in the previous subsection, there is no net magnetization in the antiferromagnetic phase. Thus, the "distinguished direction" is not defined by magnetic moments but rather by the ligands, and these are in the directions (110) and $(\bar{1}10)$. Still, the axes x and y exist, defined by the magnetic moments. These axes are inequivalent, since the localized

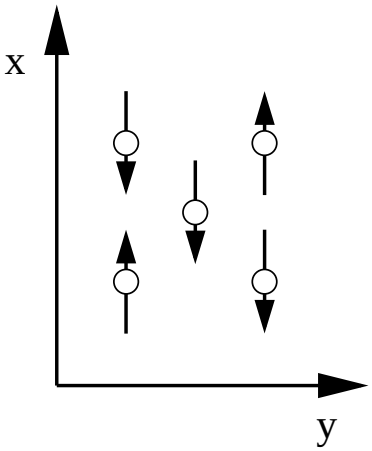

Figure 24: The antiferromagnetic surface spin configuration used to perform the analysis in the current subsection.

magnetic moments are parallel only to x. In addition, localized magnetic moments alternate along the (110) line and are kept invariant along the $(\bar{1}10)$ direction. As the spin-orbit coupling lifts the orthogonality of x and y dipoles slightly, tensor elements with the combination of indices x and y become allowed. On the other hand, the ferromagnetic tensor elements must disappear, since the contributions from opposing spins cancel each other in the antiferromagnetic phase. This leaves us with the set of tensor elements identical to the one determined by our symmetry analysis in the Chapter 2, for the AF configuration c) of the (001) surface.

As the spin-orbit coupling is intervening only once, the antiferromagnetic tensor elements are linear in the order parameter.

The above remarks about the microscopic origin of tensor elements in the AF phase suggest that the SHG is of the same order of magnitude as from a ferromagnetic surface. This means that the effect is measurable. Also, because no intersite spin-flip transitions are involved, the dynamical SHG is expected to be at least as fast as for ferromagnets.

In order to obtain quantitative conclusions about the non-vanishing tensor elements, an electronic calculation is needed. In the next sections, we present such a calculation.

3.2 The Hamiltonian

The proper description of effects encountered in transition metals and their oxides require an extensive use of correlation effects. This is evident even in some effects of the ground state [74], and becomes especially important in nonlinear optics where highly excited states are frequently involved. Therefore, we employ an exact-diagonalization method which allows for a non-perturbative treatment of electronic correlation. Under these conditions, the most general Hamiltonian has the following form:

$$H = H_{band} + H_C + H_{SO} \tag{3.2}$$

where H_{band} describes the band structure of the investigated system, H_C describes the on-site interaction, and H_{SO} is the relativistic part, which describes the spin-orbit coupling needed for magneto-optics. In this work, we focus on the on-site interaction part of the Hamiltonian, which has the following form:

$$H_C = \sum_{i,j,k,l,\sigma,\sigma',\sigma'',\sigma'''} U_{i\sigma,j\sigma',l\sigma''',k\sigma''} c^{\dagger}_{i\sigma} c^{\dagger}_{j\sigma'} c_{k\sigma''} c_{l\sigma'''} \tag{3.3}$$

Here, $U_{i\sigma,j\sigma',l\sigma''',k\sigma''}$ is the on-site Coulomb interaction which can be described in full generality by the three parameters: Coulomb repulsion U, exchange interaction J, and the

exchange anisotropy ΔJ. In this section, we will concentrate on this on-site Hamiltonian, which possesses the full spherical symmetry of a free nickel ion. The assumption is that exactly two electrons are transferred to the oxygen atom, so that the electronic configuration of the nickel ion is $3d^8 4s^0$, $3d^7 4s^1$, or $3d^6 4s^2$. The energy difference between the configurations $3d^8 4s^0$ and $3d^7 4s^1$ constitute the gap of around 4.0 eV which makes NiO a charge transfer insulator. The states most interesting for us are the 8, 7, or 6 d-states[24], or equivalently, 2, 3 or 4 holes in the d-shell of the nickel ion[25].

In this work, we will describe the holes according to the convention presented in the following table:

name	band	l_z	spin
1	3d	-2	up
2	3d	-2	down
3	3d	-1	up
4	3d	-1	down
5	3d	0	up
6	3d	0	down
7	3d	1	up
8	3d	1	down
9	3d	2	up
10	3d	2	down
11	4s	0	up
12	4s	0	down

The antisymmetrized products of the single-particle states, which constitute a basis for our many-body states, are described with the use of square brackets, e.g. [1,6] describes a two-particle state constructed of two 3_d hole states, one with $l_z = -2$, and the other with $l_z = 0$.

The states [i,j,k,l], where i...l are the single-particle states (either 3_d or 4_s), are referred to as simple product states in Fock space. The Hamiltonian H_C expressed in this basis is called by us simple-product Hamiltonian. On the other hand, Clebsch-Gordan algebra provides us with the way to obtain linear combinations of the simple-product states, these linear combinations are adapted to the spherical symmetry of the free ion and thus describe the coupled, many-body states. These many-body states form a symmetry-adapted basis for the H_C, which is then called symmetry-adapted Hamiltonian.

In the following subsections, we will describe how these holes couple to each other, forming the desired many-body states.

[24] $3d^8$, $3d^7$, or $3d^6$

[25] We do not implement point-charge model (Madelung energy) since we are not interested in the determination of the total energy in the ground state.

3.2.1 Two Holes

In the limit of weak spin-orbit coupling, two holes form a two-particle state by an LS coupling. The resulting quantum numbers are expressed as

$$\begin{aligned} L_z &= l_{z,1} + l_{z,2} \\ S_z &= s_{z,1} + s_{z,2} \end{aligned} \tag{3.4}$$

Here, the $l_{z,i}$ and $s_{z,i}$ denote the z-components of orbital and spin momenta of the i-th hole, respectively. From Eq. (3.4) it becomes clear that the orbital momentum of the coupled state constructed from two d-holes can be 0, 1, 2, 3, or 4, which is conveniently described as S, P, D, F, and G states. The resulting spin can be equal to 0 or 1, in other words each of these S - G states can have a singlet or triplet degeneracy, which is denoted as ^{1}S, ^{3}S, ^{1}P, etc.

It is necessary to take into account the fact the two holes we couple are indistinguishable. Thus, according to the Pauli principle, they have to differ by at least one quantum number. As a single d-hole can be in one of 10 states, two d-holes can produce 45 different two-particle states. Taking into account the multiplicity of the above mentioned two-particle states, both from the point of view of their total orbital momentum and their total spin, we see that the only way to fill these 45 states with our symmetry-adapted two-particle states is (^{1}S, ^{3}P, ^{1}D, ^{3}F, ^{1}G), where ^{1}X means spin-singlet and ^{3}X triplet with the corresponding orbital momentum. These symmetry-adapted states are produced from simple products with use of Clebsch-Gordan algebra, as presented in [75]. As the result, the symmetry-adapted two-particle states take the form depicted in the table A.1 in the Appendix A. The states there are named by capital letters after their angular momentum (L), their superscripts describe the spin-degeneracy (S), and subscripts refer to the magnetic quantum number (L_z). Similar nomenclature is maintained henceforth[26].

The symmetry-adapted Hamiltonian has already a diagonal form since it describes a static spherically-symmetric system. There are only five different values at the diagonal of this Hamiltonian, degenerate according to the degeneracy of two-hole symmetry-adapted wave functions which form the basis. We call these values E_S, E_P, E_D, E_F, and E_G, they can be expressed by the constants U, J, and ΔJ. We use the form of diagonal elements of the symmetry-adapted Hamiltonian as derived by Oleś and Stollhoff [76][27]. Knowing that all off-diagonal elements of the symmetry-adapted Hamiltonian (3.3) must vanish, we can express the simple-product Hamiltonian by U, J, and ΔJ. This will be used in the next subsection.

There remains an important task of determining the numerical values of the parameters U, J, and ΔJ, through which all the energies are expressed. This can be done by fitting them to measured spectroscopical lines of doubly ionized nickel in the gaseous phase. However, since only two two-hole levels are measured spectroscopically for gaseous Ni^{++} [77] (^{3}F and

[26] For three- and four-hole states, some of the states with *identical* angular momentum appear twice. We distinguish them by displaying an additional index in parenthesis.

[27] Their Hamiltonian is less general than the one described here. In particular, it does not possess the claimed spherical symmetry.

^{3}P)[28], it is not possible to determine our three parameters. On the other hand, there is another, equivalent system of parameters to describe the energy levels: Racah parameters A, B, and C [78]. Since several authors give their estimates for the values of the parameters B and C, we can express our energy levels as well as the simple-product Hamiltonian elements by Racah parameters. The values of B and C have been taken from [79], and the parameter A (equivalent to U) was adjusted to the experiment. Consequently, we obtain the following two-holes energy levels:

$$\begin{aligned} E(^3F) &= A - 8B = 0.0 \text{ eV} \\ E(^3P) &= A + 7B = 2.070 \text{ eV} \\ E(^1G) &= A + 4B + 2C = 3.008 \text{ eV} \\ E(^1D) &= A - 3B + 2C = 2.042 \text{ eV} \\ E(^1S) &= A + 14B + 7C = 7.768 \text{ eV} \end{aligned} \tag{3.5}$$

3.2.2 Three and Four Holes

In this subsection we describe the treatment of three- and four-hole states within the framework of our theory. This allows not only for the proper description of excited states in NiO, but also other materials such as CoO and FeO. The three- and four-hole states (all holes are on-site) form the basis for the Hamiltonian. Both the three-hole and four-hole parts of the Hamiltonian preserve the spherical symmetry of a free nickel ion.

The states for the ionic nickel electronic configuration $3d^7 4s$ are called three-hole states. Symmetry-adapted three-hole states are produced by coupling of symmetry-adapted two-hole states to a third d hole and performing the Clebsch-Gordan algebra followed by Gram-Schmidt orthogonalization[29]. The result is presented in Tables A.2 and A.3.

There are 120 states conveniently grouped as ^{2}P, ^{2}D, ^{2}D, ^{2}F, ^{2}G, ^{2}H, ^{4}P, and ^{4}F states according to their degeneracy in the spherical environment. The other set of 120 states results from the opposite orientation of the fourth hole, namely that in the 4s band. Although coupling of three d-holes can produce a state with angular momentum equal to 6, the Pauli principle forbids using more than two holes with the maximal l_z quantum number. Therefore the highest angular momentum is 5 (state ^{2}H), which results from using two holes with l_z=2 and one with l_z=1.

In that way we determine the basis for the three-hole symmetry-adapted Hamiltonian. Matrix elements of the three-hole simple-product Hamiltonian representation are calculated by the embedding of the matrix elements of the simple-product *two-hole* Hamiltonian. This allows us to construct the symmetry-adapted three-hole Hamiltonian using the Clebsch-Gordan algebra. As the result, the matrix elements of the symmetry-adapted Hamiltonian are expressed by Racah parameters A, B, and C and their numerical value can be calculated. This Hamiltonian is diagonal and its values are degenerate according to the multiplicity of the symmetry-adapted states.

[28] Unlike for neutral Ni (starting point for calculations on metallic nickel) where energies of two-hole states were measured.

[29] We have two *different* states of D character, they have to be orthogonal. Therefore we use *different* two-hole states to obtain these D states, and perform the orthogonalization on this (partial) result.

The symmetry-adapted four-hole states (i.e. states $3d^6 4s^2$) are obtained by a Clebsch-Gordan coupling of the two-hole states, followed by Gram-Schmidt orthogonalization. The result of this numerically performed procedure is a set of 210 states ^{1}S, ^{1}S, ^{1}D, ^{1}D, ^{1}F, ^{1}G, ^{1}G, ^{1}I, ^{3}P, ^{3}P, ^{3}D, ^{3}F, ^{3}F, ^{3}G, ^{3}H, and ^{5}D presented in Table A.4. The highest angular momentum possible to obtain by coupling four undistinguishable d-holes is 6, since one has to use two holes with l_z=2 and two with l_z=1. As previously, the matrix elements of the four-hole simple-product Hamiltonian are determined by use of an embedding procedure, they are then used to construct the four-hole symmetry-adapted Hamiltonian. Again, it is diagonal and its values are degenerate according to the multiplicity of the symmetry-adapted states. The resulting Hamiltonian fully describes the three- and four-hole interactions.

The procedure presented here was performed for a specific system, nickel ion. Nevertheless, it can be applied to any system where up to four d-holes or d-electrons are present (the parameter values must be altered), like cobalt, iron, scandium, titanium or vanadium. Furthermore, an extension towards the systems with 5 d-electrons is possible - one has to couple an additional hole to our four-hole states and orthogonalize the result. For the elements of such five-hole Hamiltonian, an embedding procedure similar to the one described by us can then be performed.

3.2.3 Bulk vs. Surface of NiO

So far, we have discussed the on-site interaction part of the Hamiltonian in the spherically symmetric environment. Because of this symmetry, the Hamiltonian is degenerate to a large extent. Nearly all these degeneracies are lifted when the symmetry is lowered. Since the nonlinear magneto-optic effects are known to be sensitive to the splitting of electronic levels [80], we examine the crystal field induced level splitting in detail. Here, we will show how the lowering of the symmetry influences the two-hole part of our Hamiltonian. The extension of the analysis to three- and four-hole parts of the Hamiltonian is straightforward.

Spherical	O_h	C_{4v}
^{1}S	^{1}A$_1$	^{1}A$_1$
^{3}P	^{3}T$_1$	^{3}A$_1$+^{3}E
^{1}D	^{1}E	^{1}A$_1$+^{1}B$_1$
	^{1}T$_2$	^{1}B$_2$+^{1}E
^{3}F	^{3}A$_2$	^{3}B$_2$
	^{3}T$_1$	^{3}A$_1$+^{3}E
	^{3}T$_2$	^{3}B$_1$+^{3}E
^{1}G	^{1}A$_1$	^{1}A$_1$
	^{1}E	^{1}A$_1$+^{1}B$_1$
	^{1}T$_1$	^{1}A$_2$+^{1}E
	^{1}T$_2$	^{1}B$_2$+^{1}E

Table 3.1: Splitting of the spherical symmetry-adapted states in the cubic (O_h) and square (C_{4v}) environments.

First, we will describe the level splitting in the cubic environment. The levels obtained in this way will be split in the next step which involves lowering the symmetry from cubic to square one due to the surface.

For example, the ^{3}F state gets split in the cubic environment into states with symmetry ^{3}A$_2$, ^{3}T$_1$, and ^{3}T$_2$. These states are constructed by linear combinations of the previously defined symmetry-adapted orbitals. Such linear combinations of spherical functions, adapted to the cubic environment, are called *cubic harmonics*. Using them, we describe the states in the cubic and square (surface) environment. The presence of the surface with its square symmetry splits the states further, one obtains the following set of two-hole surface states: ^{3}E, ^{3}A$_2$, ^{3}B$_2$, ^{3}E, and ^{3}B$_1$. Splitting of all the two-hole states in consequent symmetry breaking is presented in the

Table 3.1.

Level splitting due to lowering of the symmetry is governed by the rules of group theory. In particular, it tells us that, for a cubic symmetry O_h, only representations of the order up to three are possible. The highest order of representations which describe the surface states (where the surface square lattice has symmetry C_{4v}) is two. These conditions mark the maximal orbital degeneracies. The particular assignment of the cubic harmonics to the states in the cubic and square environments can be performed by careful analysis of the symmetry properties of the harmonics and the representations.
The square symmetry-adapted wavefunctions for each of the surface two-hole states are presented in Table 3.2.

Table 3.2: Two-hole wavefunctions adapted to surface symmetry. The two 4s holes have been skipped in the notation. For the triplets, only the $\uparrow\uparrow$ state is shown, but the remaining ones can be obtained easily.

Spherical state	Surface state	Wavefunction
^{1}S	^{1}A$_1$	$\sqrt{\frac{1}{5}} \times \big([1,10] - [3,8] + [5,6] + [4,7] - [2,9]\big)$
^{3}P	A$_1$	$\sqrt{\frac{4}{5}}[1,9] - \sqrt{\frac{1}{5}}[3,7]$
	E$_\alpha$	$\sqrt{\frac{2}{5}}[1,7] - \sqrt{\frac{3}{5}}[3,5]$
	E$_\beta$	$-\sqrt{\frac{2}{5}}[3,9] + \sqrt{\frac{3}{5}}[5,7]$
^{1}D	A$_1$	$\sqrt{\frac{2}{7}}[1,10] + \sqrt{\frac{1}{14}}[3,8] - \sqrt{\frac{2}{7}}[5,6] +$ $-\sqrt{\frac{1}{14}}[4,7] - \sqrt{\frac{2}{7}}[2,9]$
	B$_1$	$-\sqrt{\frac{1}{7}}[6,9] - \sqrt{\frac{3}{14}}[7,8] + \sqrt{\frac{1}{7}}[5,10] + \sqrt{\frac{1}{7}}[1,6] +$ $-\sqrt{\frac{3}{14}}[3,4] - \sqrt{\frac{1}{7}}[2,5]$
	B$_2$	$-\sqrt{\frac{1}{7}}[6,9] - \sqrt{\frac{3}{14}}[7,8] + \sqrt{\frac{1}{7}}[5,10] - \sqrt{\frac{1}{7}}[1,6] +$ $+\sqrt{\frac{3}{14}}[3,4] + \sqrt{\frac{1}{7}}[2,5]$
	E$_\alpha$	$\sqrt{\frac{3}{7}}[1,8] - \sqrt{\frac{1}{14}}[3,6] + \sqrt{\frac{1}{14}}[4,5] - \sqrt{\frac{3}{7}}[2,7]$
	E$_\beta$	$\sqrt{\frac{3}{7}}[4,9] - \sqrt{\frac{1}{14}}[6,7] + \sqrt{\frac{1}{14}}[5,8] - \sqrt{\frac{3}{7}}[3,10]$

continued on the next page

continued from the previous page		
	B_1	$\sqrt{\frac{1}{2}}\big([1,5]-[5,9]\big)$
	E_α	$\sqrt{\frac{1}{8}}\big(\sqrt{3}[7,9]+\sqrt{3}[1,7]+\sqrt{2}[3,5]\big)$
^3F	E_β	$-\sqrt{\frac{1}{8}}\big(\sqrt{3}[1,3]+\sqrt{3}[3,9]+\sqrt{2}[5,7]\big)$
	B_2	$-\sqrt{\frac{1}{2}}\big([1,5]+[5,9]\big)$
	A_2	$\sqrt{\frac{1}{5}}[1,9]+\sqrt{\frac{4}{5}}[3,7]$
	E_γ	$-\sqrt{\frac{1}{8}}\big(\sqrt{5}[1,3]-\sqrt{\frac{9}{5}}[3,9]-\sqrt{\frac{6}{5}}[5,7]\big)$
	E_δ	$-\sqrt{\frac{1}{8}}\big(-\sqrt{5}[7,9]+\sqrt{\frac{9}{5}}[1,7]+\sqrt{\frac{6}{5}}[3,5]\big)$
	$A_{1\alpha}$	$\sqrt{\frac{7}{12}}\big(\sqrt{\frac{1}{70}}[1,10]+\sqrt{\frac{8}{35}}[3,8]+\sqrt{\frac{18}{35}}[5,6]-\sqrt{\frac{8}{35}}[4,7]+$ $-\sqrt{\frac{1}{70}}[2,9]\big)+\sqrt{\frac{5}{24}}[9,10]+\sqrt{\frac{5}{24}}[1,2]$
	$A_{1\beta}$	$-\sqrt{\frac{5}{12}}\big(\sqrt{\frac{1}{70}}[1,10]+\sqrt{\frac{8}{35}}[3,8]+\sqrt{\frac{18}{35}}[5,6]-\sqrt{\frac{8}{35}}[4,7]+$ $-\sqrt{\frac{1}{70}}[2,9]\big)+\sqrt{\frac{7}{24}}[9,10]+\sqrt{\frac{7}{24}}[1,2]$
	B_1	$-\sqrt{\frac{3}{28}}[6,9]+\sqrt{\frac{2}{7}}[7,8]+\sqrt{\frac{3}{28}}[5,10]+\sqrt{\frac{3}{28}}[1,6]+$ $+\sqrt{\frac{2}{7}}[3,4]-\sqrt{\frac{3}{28}}[2,5]$
^1G	A_2	$\sqrt{\frac{1}{2}}[9,10]-\sqrt{\frac{1}{2}}[1,2]$
	E_α	$\sqrt{\frac{1}{8}}\big(\sqrt{\frac{1}{2}}[7,10]-\sqrt{\frac{1}{2}}[8,9]+\sqrt{\frac{1}{2}}[1,8]+\sqrt{3}[3,6]+$ $-\sqrt{3}[4,5]-\sqrt{\frac{1}{2}}[2,7]\big)$
	E_β	$\sqrt{\frac{1}{8}}\big(\sqrt{\frac{1}{2}}[2,3]-\sqrt{\frac{1}{2}}[1,4]+\sqrt{\frac{1}{2}}[4,9]+\sqrt{3}[6,7]+$ $-\sqrt{3}[5,8]-\sqrt{\frac{1}{2}}[3,10]\big)$
	B_2	$\sqrt{\frac{1}{2}}\big(-\sqrt{\frac{3}{14}}[6,9]+\sqrt{\frac{4}{7}}[7,8]-\sqrt{\frac{3}{14}}[5,10]-\sqrt{\frac{3}{14}}[1,6]+$ $-\sqrt{\frac{4}{7}}[3,4]+\sqrt{\frac{3}{14}}[2,5]\big)$
	E_γ	$\sqrt{\frac{1}{8}}\big(-\sqrt{\frac{1}{14}}[4,9]-\sqrt{\frac{3}{7}}[8,9]+\sqrt{\frac{3}{7}}[5,8]+\sqrt{\frac{1}{14}}[3,10]+$ $+\sqrt{\frac{7}{2}}[2,3]-\sqrt{\frac{7}{2}}[1,4]\big)$
	E_δ	$\sqrt{\frac{1}{8}}\big(\sqrt{\frac{7}{2}}[7,10]-\sqrt{\frac{7}{2}}[8,9]-\sqrt{\frac{1}{14}}[1,8]-\sqrt{\frac{3}{7}}[3,6]+$ $+\sqrt{\frac{3}{7}}[4,5]+\sqrt{\frac{1}{14}}[2,7]\big)$

Having determined the surface states, we need to obtain the corresponding energy levels. For the levels resulting from the split ^3F state, these energies are known from the experiment [81] and presented in Table 3.3. In order to obtain the energies for the other levels we use a ligand field approach.

First, we have to express all the surface states in terms of the square surface ligand

parameters ε_0, D_q, D_S, and D_U[30]. This is done in a manner similar to the one described in [78] for the cubic symmetry, but we have to account for the different (lower) symmetry of the ligand field. The result is presented in Table A.5. An interesting remark is that setting the surface-characteristic parameters D_U and D_S as equal to zero increases the degeneracy of the states. The degeneracy is then characteristic to the cubic environment, as presented in the second column of the Table 3.1. Setting also the cubic ligand parameters ε_0 and D_q to zero leads the levels back to the spherical symmetry.

In principle, knowing the position of the ligands for our particular material, and approximating the ligands by either point charges or dipoles, we can calculate these parameters. Instead, we use the experimental knowledge and fit these parameters so that the energies of the states resulting from splitting of the ^{3}F state are expressed correctly. We obtain the following values for the parameters:

$$\begin{aligned} \varepsilon_0 &= 0.6699 \text{ eV} \\ D_q &= -0.1633 \text{ eV} \\ D_S &= 1.6542 \text{ eV} \\ D_U &= 0.2633 \text{ eV} \end{aligned} \tag{3.6}$$

The parameters obtained in this way allow for determination of the energy shifts caused by the symmetry breaking. The level energies obtained in this way are presented in Table A.5. They find a confirmation in experiments [82]. Along with the energies determined in the previous subsection for the spherically symmetric states, this gives us the full knowledge about the eigenfunctions and eigenvalues of energy at the surface of NiO.

$^3B_1$	0.0 eV
^3E	0.65 eV
$^3B_2$	1.0 eV
$^3A_2$	1.3 eV
^3E	1.44 eV

Table 3.3: Experimental values of energy levels for the surface-symmetry split ^{3}F state [81].

Clearly, the ligand field parameters are smaller than the electron correlation parameter U (about 13.0 eV). Since the energy levels for two- and three-hole states are separated by U (in the spherically symmetrical environment), we do not expect any overlap of these states also in the lower symmetries.

In the next two sections we will use these functions and energies to calculate the nonlinear optical spectra of NiO and to draw some conclusions about spin- and charge dynamics in this material.

3.3 The Nonlinear Spectrum of NiO (001)

According to eq. (3.1), there are three components needed for our calculations of the nonlinear susceptibility tensor elements: wavefunctions of our many-body eigenstates, transition matrix elements between these states, and the energy levels of these states. The wavefunctions and the corresponding energies were derived in the previous sections. However,

[30] Among these parameters, ε_0 describes the energy shift in the crystal field, D_q is the level splitting in the cubic environment, D_S and D_U correspond to the level splitting in the octahedral and C_{4v} symmetries, respectively.

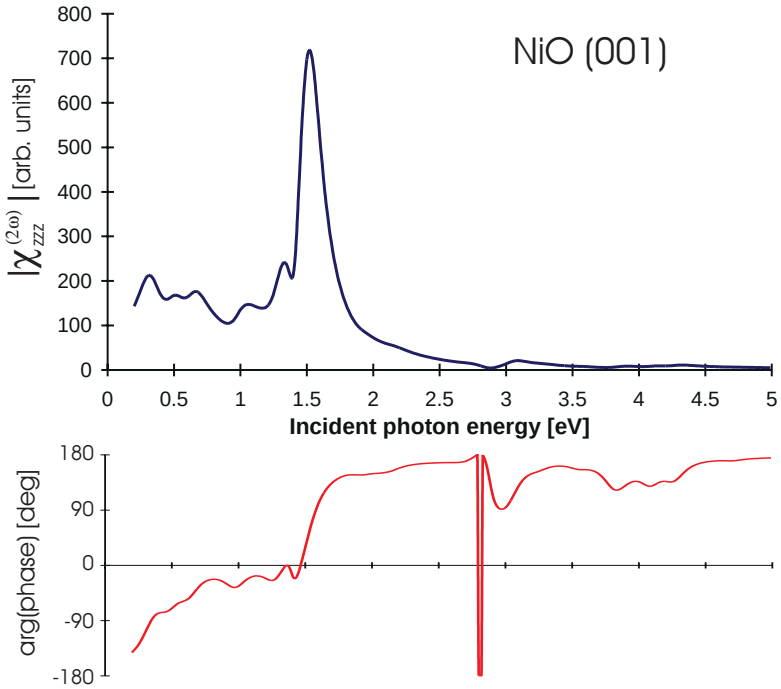

Figure 25: Spectrum of the paramagnetic tensor element χ_{zzz}. Both magnitude and the argument of the complex phase of the tensor element are presented separately.

the exact calculation of the transition matrix elements is very unreliable (transition metal oxides constitute the most difficult case due to their strong electronic correlations) and will not be performed within the framework of the current theory. Instead, we will use the approximations for the transition matrix elements obtained by Hübner *et al.* [73], which constitute the selection rules. Here, we present the spectra of two tensor elements: the prototypic paramagnetic tensor element χ_{zzz} in Fig. 25 and the prototypic antiferromagnetic tensor element χ_{zxy} in Fig. 26.

In the spectrum of χ_{zzz}, all the features fall within the gap, which we assume at 4.0 eV. The dominant structure in the spectrum corresponds to the transitions from the ground state to the states resulting from the split ^{3}P state, which are all located near 3.0 eV. The position of the peak, around 1.5 eV corresponds to the fact that the tensor describes a two-photon process. Other, smaller peaks related to transitions between various states are also present. Another important feature of the calculated spectrum is that the tensor element is complex and its phase varies. This has important consequences for the absence of time-reversal symmetry in the process of SHG, as already extensively discussed in Sec. 2.4.

The spectrum of the antiferromagnetic tensor element χ_{zxy} reveals similar main traits as the previously discussed spectrum. However, we can observe an additional peak at 0.6 eV, with intensity much higher than the corresponding feature in the spectrum of the paramagnetic tensor element χ_{zzz}. Consequently, this is the "antiferromagnetic" spectral line which we suppose is especially suitable for nonlinear magneto-optics. Another inter-

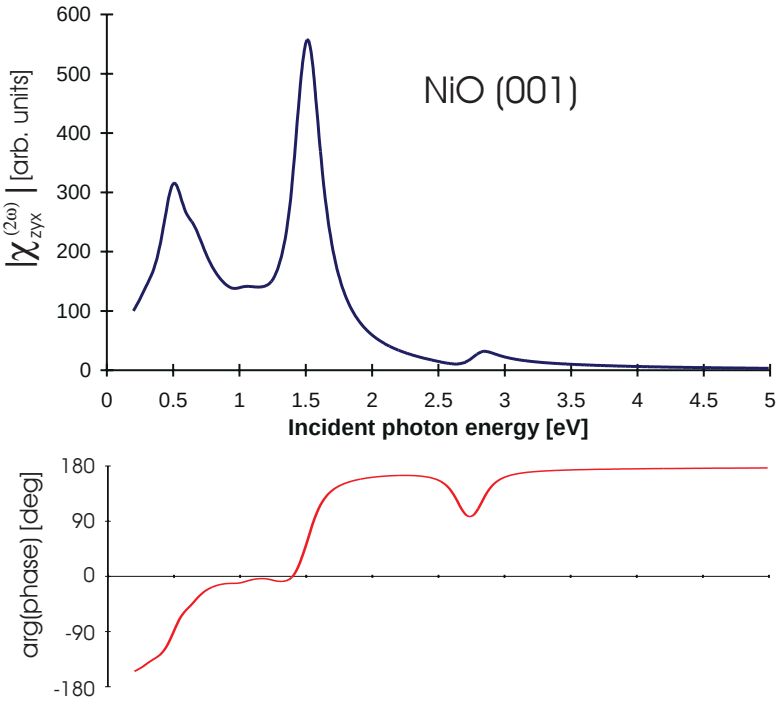

Figure 26: Spectrum of the antiferromagnetic tensor element χ_{zyx}. Both magnitude and the argument of the complex phase of the tensor element are presented separately.

esting result is that both tensor elements are of similar magnitude. This is a favorable condition for the antiferromagnetic domain imaging. Taking into account the magnitudes of both tensor elements presented in this section, domain contrast should be as large as in ferromagnets (where it is of the order of *unity* in SHG).

The results described here concern the process of static SHG, i.e. a measurement taken on a sample close to thermodynamic equilibrium. In the next section, we will describe our anticipations as to the dynamical (time-resolved) measurements of highly excited states in nickel oxide.

3.4 Spin and Charge Dynamics

The area of dynamics of magnetic materials on femto-second timescales escaped scientifical investigations till very recently, both from theoretical and experimental point of view. However, the importance of understanding the dynamics in view of new challenges for the materials needed for storage and computer memory media becomes obvious. Only very recently seminal experimental works have been performed in the sub-picosecond regime for *ferromagnetic* materials [83, 84, 85, 86]. The very fact of the observed spin dynamics at these short timescales fostered the development of appropriate theoretical models, since the the spin-lattice relaxation processes, appearing at the timescales of several tens to hundreds of picoseconds [87] cannot be responsible for the observed effect. The con-

cept of different temperatures (charge, spin, and lattice temperature) used to explain the results [83, 84] is not strictly valid, since at so short timescales it is impossible to define a temperature, which is rather an equilibrium property. A proper models, dynamics of complex populations, have been developed for both linear [88] and nonlinear [89] magneto-optics from ferromagnets. However, the investigations of femtosecond spin-dynamics of antiferromagnets is nonexisting so far.

Here, we describe the simulation of an SHG pump-and-probe experiment in NiO. During such an experiment, the sample is excited by a strong laser pulse, and then (with a variable delay of several tens to hundreds of femtoseconds) the second - probe - pulse is issued. The SHG response of the sample to this second beam is measured and can reveal the dynamic properties of the sample. In this section, we

- describe the theoretical model for the dynamics and
- present and discuss the results of the calculations.

3.4.1 Treatment of Pump-Probe Experiments

In our work we extend the theory for probing the femtosecond spin-dynamics by means of nonlinear optics towards antiferromagnets. In fact, we choose the same approach as in [89] and add the initial excited state preparation and the dynamics of complex populations to our previously described theory of the static SHG response. The initial excitation is infinitesimally short in time (the excitation pulse is already completed when our dynamics starts) but its energy distribution follows a Gaussian profile, centered at 2 eV and with the width of 20 eV (truncated at 0 eV, so that no negative energies appear). This width of excitation allows us to probe the fast limit of the dynamics, since all the energy levels (including the highest) are populated and consequently all the de-excitation channels are open. The restriction of the Hamiltonian to electronic on-site interactions complies with this limit. Consequently, the excitation populates all the many-body states of our system, and then these states are left to evolve freely. Under these circumstances the time-dependent tensor element χ_{ijk} can be expressed as

$$\chi^{(2)}_{ijk}(2\mathbf{q},2\omega) = \frac{e^3}{2q^3V}\sum_{\mathbf{k},l,l',l''}\Bigg[\langle \mathbf{k}+2\mathbf{q},l''|i|\mathbf{k}l\rangle\langle \mathbf{k}l|j|\mathbf{k}+\mathbf{q},l'\rangle\langle \mathbf{k}+\mathbf{q},l'|k|\mathbf{k}+2\mathbf{q},l''\rangle \times \\ \times \frac{\frac{p(E_{\mathbf{k}+2\mathbf{q},l''},t)-p(E_{\mathbf{k}+\mathbf{q},l'},t)}{E_{\mathbf{k}+2\mathbf{q},l''}-E_{\mathbf{k}+\mathbf{q},l'}-\hbar\omega+i\hbar\alpha} - \frac{p(E_{\mathbf{k}+\mathbf{q},l'},t)-p(E_{\mathbf{k}l},t)}{E_{\mathbf{k}+\mathbf{q},l'}-E_{\mathbf{k}l}-\hbar\omega+i\hbar\alpha}}{E_{\mathbf{k}+2\mathbf{q},l''}-E_{\mathbf{k}l}-2\hbar\omega+2i\hbar\alpha}\Bigg], \quad (3.7)$$

Here, $p(E_{\mathbf{k}l},t) = \langle\Psi(t)|kl\rangle = f(E)\times e^{-\frac{i}{\hbar}E_{\mathbf{k},l}t}$, and the rest of symbols are the same as in Eq. (3.1). The time evolution of the system exclusively results from the presence of the quantum phase factor. Broadening of many-body levels does not occur since the many-body Hamiltonian is diagonal due to the choice of the appropriate symmetry-adapted basis (as described in Sec. 3.2). Consequently, the effect described by us has a purely quantum nature and cannot be explain within a classical theory. As previously, the band structure is

neglected due to very small dispersion of the gap states which are involved in the described process. In the next subsection we present the results of the numerical simulations of the spin dynamics.

3.4.2 Relaxation of Excited States

In this subsection, we present for the first time the femtosecond dynamics of the antiferromagnetic order parameter, represented by the antiferromagnetic tensor element χ_{zyx}. As it is clear from the Fig. 27a, there is no decay of the tensor element, like for the metallic systems. The coherence is preserved for a long time (until phenomena neglected within this framework take place, like phonon-magnon coupling), which manifests itself by beating repeated regularly every 50 fs. Fig. 27b presents a zoom into such a period of 50 fs, it demonstrates that the spin dynamics takes place within femtoseconds, and thus is not slower than in metals.

For comparison, we have also performed similar calculations for the paramagnetic tensor element χ_{zzz}. The results are shown in Fig. 28. The basic features are very similar to the dynamics of the antiferromagnetic tensor element described previously. The ultimate limit of the charge dynamics lies also within several femtoseconds, as it can be seen in Fig. 28b, and the coherence is preserved for a long time.

The coherence of the tensor elements determining the SHG response of the AF surface may be destroyed by the phonons, which were neglected in the current framework. As mentioned above, the phonon-magnon coupling intervenes within several tens of picoseconds. Consequently, the coherence times are four orders of magnitude longer than the ultimate speed of the spin and charge dynamics. Additional interactions, like electron-electron interactions of the nearest neighbors, band structure (hopping), or phonons, can bring decoherence. The question if this decay really occurs when these effects are taken into account remains open. However, by choice of a particular spectral line instead of the spectrally wide initial excitation described here one can make the coherence last longer (typical widths of spectral lines in oxides are in the range of tens of μeV [5], which corresponds to several picoseconds coherence times).

The situation where the elementary dynamics happens within femtoseconds and coherence is preserved beyond hundreds of femtoseconds is very favorable for the magneto-optic storage and quantum computing applications [90], since the spin dynamics determines the write and readout speed. Till now, only semiconductors have been known to fulfill this criterion, however the applications of those materials suffer from problems related to spin injection [91]. In the antiferromagnetic oxides no spin injection is necessary since the magnetic moments are already there.

This conclusion ends the description of the results of our femtosecond spin- and charge-dynamics. In the last chapter of this dissertation, we will present other conclusions, preceded by a brief summary of our results.

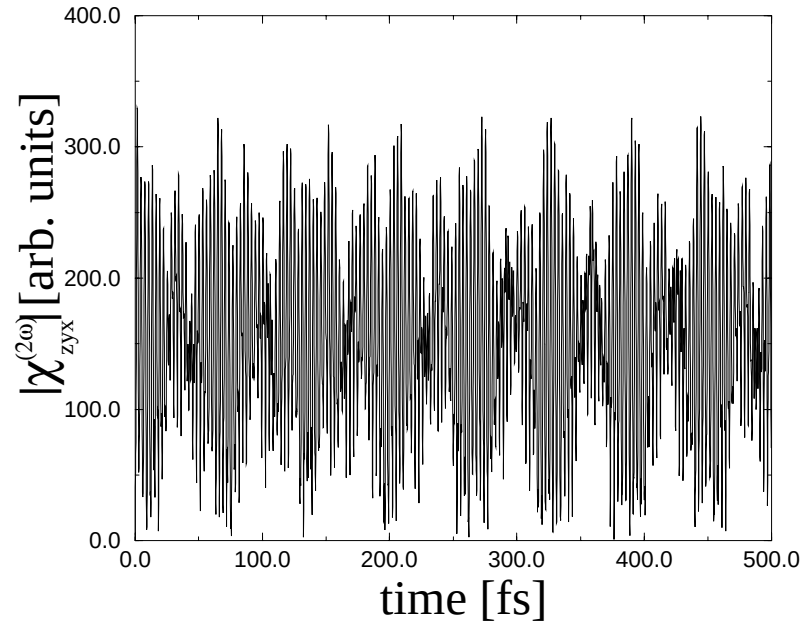

a

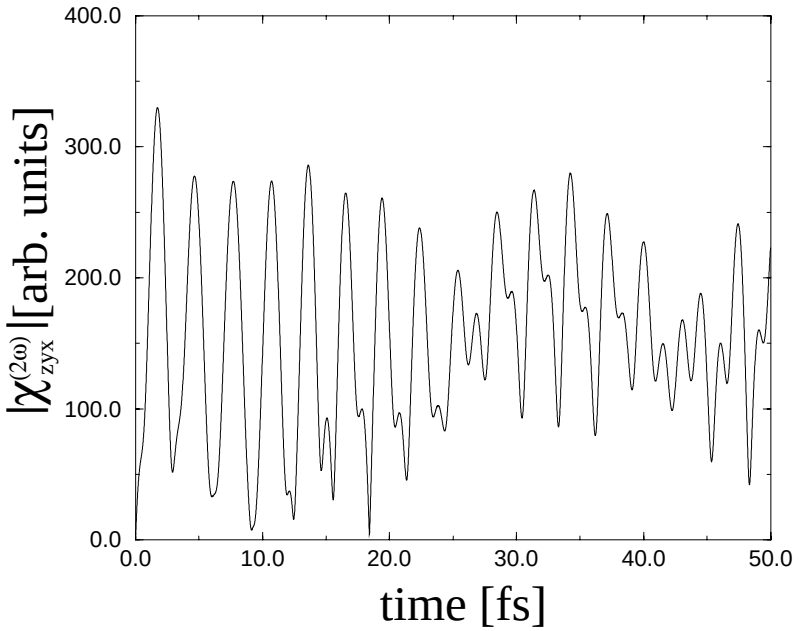

b

Figure 27: Dynamics of the antiferromagnetic tensor element χ_{zyx} on NiO (001) within 500 fs (a) and 50 fs (b). The incident photon energy of the probe pulse $\hbar\omega$=1.44 eV. The graphs present the magnitude of the complex tensor element.

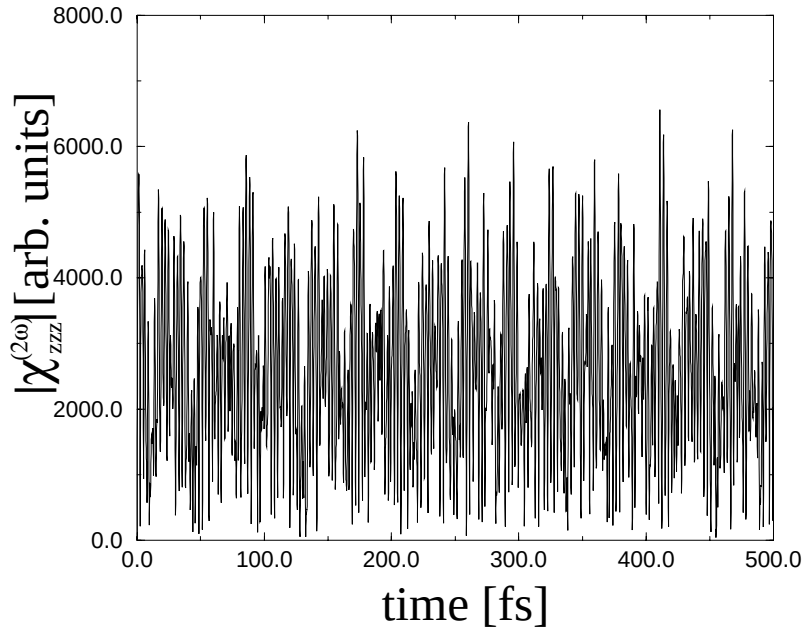

a

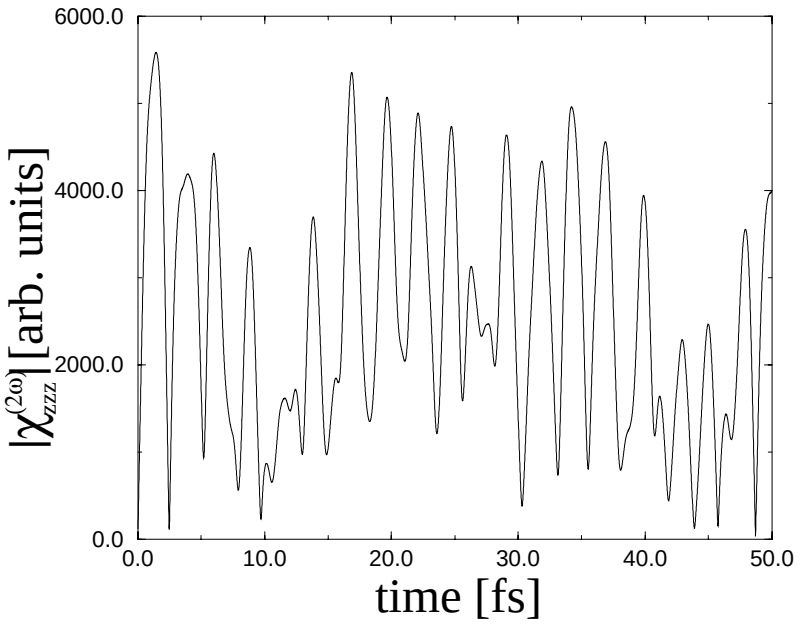

b

Figure 28: Dynamics of the paramagnetic tensor element χ_{zzz} on NiO (001) within 500 fs (a) and 50 fs (b). The incident photon energy of the probe pulse $\hbar\omega$=1.44 eV. The graphs present the magnitude of the complex tensor element.